CANCER RESEARCH | TUMOR BIOLOGY AND IMMUNOLOGY

Enhanced Efficacy of Simultaneous PD-1 and PD-L1 Immune Checkpoint Blockade in High-Grade Serous Ovarian Cancer

Changxin Wan[1,2], Matthew P. Keany[3,4], Han Dong[3,5], Linah F. Al-Alem[6,7], Unnati M. Pandya[6,7], Suzan Lazo[3,4], Karsten Boehnke[8], Katherine N. Lynch[4,9], Rui Xu[6,7,10], Dominique T. Zarrella[6], Shengqing Gu[1], Paloma Cejas[4,11], Klothilda Lim[4,11], Henry W. Long[4,11], Kevin M. Elias[7,12], Neil S. Horowitz[7,12], Colleen M. Feltmate[7,12], Michael G. Muto[7,12], Michael J. Worley Jr[7,12], Ross S. Berkowitz[7,12], Ursula A. Matulonis[4,13], Marisa R. Nucci[14,15], Christopher P. Crum[14,15], Bo R. Rueda[6,7,16], Myles Brown[4,9,11], Xiaole Shirley Liu[1,11], and Sarah J. Hill[4,9,14,15]

ABSTRACT

Immune therapies have had limited efficacy in high-grade serous ovarian cancer (HGSC), as the cellular targets and mechanism(s) of action of these agents in HGSC are unknown. Here we performed immune functional and single-cell RNA sequencing transcriptional profiling on novel HGSC organoid/immune cell co-cultures treated with a unique bispecific anti-programmed cell death protein 1 (PD-1)/programmed death-ligand 1 (PD-L1) antibody compared with monospecific anti-PD-1 or anti-PD-L1 controls. Comparing the functions of these agents across all immune cell types in real time identified key immune checkpoint blockade (ICB) targets that have eluded currently available monospecific therapies. The bispecific antibody induced superior cellular state changes in both T and natural killer (NK) cells. It uniquely induced NK cells to transition from inert to more active and cytotoxic phenotypes, implicating NK cells as a key missing component of the current ICB-induced immune response in HGSC. It also induced a subset of CD8 T cells to transition from naïve to more active and cytotoxic progenitor-exhausted phenotypes post-treatment, revealing the small, previously uncharacterized population of CD8 T cells responding to ICB in HGSC. These state changes were driven partially through bispecific antibody-induced downregulation of the bromodomain-containing protein BRD1. Small-molecule inhibition of BRD1 induced similar state changes *in vitro* and demonstrated efficacy *in vivo*, validating the co-culture results. Our results demonstrate that state changes in both NK and a subset of T cells may be critical in inducing an effective anti-tumor immune response and suggest that immune therapies able to induce such cellular state changes, such as BRD1 inhibitors, may have increased efficacy in HGSC.

Significance: This study indicates that increased efficacy of immune therapies in ovarian cancer is driven by state changes of NK and small subsets of CD8 T cells into active and cytotoxic states.

Introduction

High-grade serous ovarian cancer (HGSC) is the fifth leading cause of cancer death in women in the United States (1). Patients are diagnosed at late stage due to limited early detection methods, and are typically treated with combinations of surgery and chemotherapy (2). Though immune checkpoint blockade (ICB) agents demonstrate success in other solid tumor types, monospecific ICB antibodies exhibit minimal efficacy in HGSC (3, 4). Many theories explore the contributions of different immune cell types to HGSC outcome and possibly ICB response. Poor HGSC outcomes associate with an increased proportion of tumor-associated macrophages (5). Positive outcomes associate with increased ratios of CD8 T cells to CD4 Tregs (6, 7) and increased fractions of natural killer (NK) cells in ascites (8, 9). Limited mechanistic data explain these findings. On the basis of work in ICB-responsive solid tumor types, it is likely that the quality of the T and NK cells, rather than their quantity, matters in eliciting ICB activity (10, 11).

---

[1]Department of Data Sciences, Dana-Farber Cancer Institute, Harvard T.H. Chan School of Public Health, Boston, Massachusetts. [2]Program in Computational Biology and Bioinformatics, Duke University, Durham, North Carolina. [3]Department of Cancer Immunology and Virology, Dana-Farber Cancer Institute, Boston, Massachusetts. [4]Department of Medical Oncology, Dana-Farber Cancer Institute, Boston, Massachusetts. [5]Department of Microbiology and Immunology, Harvard Medical School, Boston, Massachusetts. [6]Vincent Center for Reproductive Biology, Department of Obstetrics and Gynecology, Massachusetts General Hospital, Boston, Massachusetts. [7]Obstetrics Gynecology and Reproductive Biology, Harvard Medical School, Boston, Massachusetts. [8]Oncology Translational Research, Eli Lilly and Company, New York, New York. [9]Division of Molecular and Cellular Oncology, Dana-Farber Cancer Institute, Boston, Massachusetts. [10]Department of Internal Medicine, Shaanxi Province Cancer Hospital, Affiliated Hospital of Medical College of Xi'an Jiaotong University, Xi'an, Shaanxi, P.R. China. [11]Center for Functional Cancer Epigenetics, Dana-Farber Cancer Institute, Boston, Massachusetts. [12]Division of Gynecologic Oncology, Department of Obstetrics and Gynecology, Brigham and Women' Hospital, Boston, Massachusetts. [13]Department of Medicine, Brigham and Women's Hospital, Boston, Massachusetts. [14]Department of Pathology, Brigham and Women's Hospital, Boston, Massachusetts. [15]Department of Pathology, Harvard Medical School, Boston, Massachusetts. [16]Division of Gynecologic Oncology, Department of Obstetrics and Gynecology, Massachusetts General Hospital, Boston, Massachusetts.

Note: Supplementary data for this article are available at Cancer Research Online (http://cancerres.aacrjournals.org/).

Corresponding Author: Sarah J. Hill, Dana-Farber Cancer Institute, Smith 834, 450 Brookline Ave., Boston, MA 02215. Phone: 617-272-5451; Fax: 617-582-8601; E-mail: sarah_hill@dfci.harvard.edu

Cancer Res 2021;81:158–73

doi: 10.1158/0008-5472.CAN-20-1674

©2020 American Association for Cancer Research.

In most solid tumors, the tumor microenvironment induces dysfunction in T and possibly NK cells (12, 13). In CD8 T cells, this dysfunction, called "exhaustion," is mediated by stable epigenetic reprogramming producing subsets of differentially functional cells including progenitor-exhausted and terminally exhausted T cells (10, 14, 15). The contribution of naïve versus exhausted CD8 T-cell subsets to ICB response, and the mechanism of NK-cell dysfunction and ICB-triggered response, are still being defined in all solid tumor types, including HGSC (10, 11, 13, 16).

A better understanding of cells critical for ICB response in HGSC and the effect of cell state on their response to ICB agents is needed. Organoid co-cultures containing patient-matched tumor and all intratumoral immune cells represent a human model that can be studied over time using ICB treatments to ask questions about ICB efficacy and mechanism of action (17, 18).

Here we utilize short-term patient-derived HGSC organoid co-cultures containing tumor organoids and the full complement of intratumoral immune cells to functionally assess the mechanism of action of ICB agents in every type of immune cell in the culture. To detect key cellular and mechanistic targets evading current therapies, we compared the action of a novel bispecific anti-programmed cell death protein 1 (PD-1)/programmed death-ligand 1 (PD-L1) ICB antibody (19) with its monospecific anti-PD-1 and anti-PD-L1 controls. We show that the bispecific antibody uniquely induces state changes in NK cells from inert to active states and most strongly induces a state change in CD8 T cells from naïve to cytotoxic progenitor-exhausted states, with neither target previously demonstrated as critical for ICB response in HGSC. We demonstrate that both state changes are driven partially through downregulation of the bromodomain-containing protein BRD1. BRD1 inhibition by a small-molecule inhibitor, BAY-299, recapitulates these state changes for T and NK cells *in vitro* and *in vivo*, and demonstrates efficacy *in vivo*, thereby validating the co-culture results and suggesting BRD1 as a possible immune therapy target. Taken together our data indicate that efficacy of immune therapies in HGSC can be driven by transition of NK-cell and CD8 T-cell subsets into active and cytotoxic states likely through epigenetic changes driven, in part, by BRD1 downregulation or inhibition removing some tumor microenvironment driven dysfunction.

Materials and Methods

For additional and detailed materials and methods, please see Supplementary Materials and Methods.

Patient samples

HGSC tumor tissue was collected from 12 patients undergoing primary debulking surgery at Brigham and Women's Hospital (BWH, Boston, MA) and Dana-Farber Cancer Institute (DFCI, Boston, MA) for organoid co-culture generation and functional testing between December 2019 and April 2020. Tumor tissue from patient 20-22 was obtained under BWH/Partners Institutional Review Board (IRB)–approved discarded tissue protocol 2016P000559. Written informed consent was obtained for the remaining subjects on either BWH/Partners IRB–approved protocol 2016P002819 or DFCI IRB–approved protocol 02-051. All studies in this work were conducted in accordance with the U.S. Common Rule and Belmont Report and approved by the DFCI and BWH/Partners IRBs.

Co-culture generation

Tumors were mechanically dissociated, diluted in DMEM (Life Technologies, catalog no. 11965-092), 10% FBS (Sigma, catalog no. F2442-500), 1% penicillin streptomycin (Life Technologies, catalog no. 15140-122), and 2.5 mg/mL Type II Collagenase (Life Technologies, catalog no. 17101015), and shaken on a horizontal platform for 20 minutes at 37°C. The homogenate was filtered through a 100 μm filter (Corning, catalog no. 352360), pelleted, and washed in 1× Red Blood Cell Lysis Buffer (BioLegend, catalog no. 420301). The cells were then resuspended in DMEM/10% FBS, counted, and diluted to a concentration of 6×10^6 cells (or organoids)/mL in DMEM, 10% FBS, 1% Pen/Strep, and 30 ng/mL of IL2 (PeproTech, catalog no. 200-02) mixed with 15% Matrigel (Corning, catalog no. 356231). This cell suspension was then plated into 48-well plates (USA Scientific, catalog no. CC7672-7548) at 40 μL per well and incubated at 37°C to allow for settling, then drug containing media was added to each well. All drug preparations were prepared in DMEM, 10% FBS, 1% Pen/Strep, and 30 ng/mL of IL2. Drugs included Anti-PD-1 (Selleck, catalog no. A2005), IgGEn Isotype Control (provided by Eli Lilly), anti-PD-L1 (LY3300054), bispecific anti-PD-1/PD-L1 (LY3434172; all antibodies used at 10 μg/mL), and BAY-299 (MedChemExpress, catalog no. HY-107424; used at 1 μmol/L). Co-cultures were harvested 96 hours after plating for all functional assays detailed in the Supplementary Methods.

Single-cell RNA sequencing

Single-cell RNA sequencing (scRNA-seq) experiments were performed by the BWH Single Cell Genomics Core. For scRNA-seq analysis of the organoid co-cultures, viable $CD45^+$ cells from organoid co-cultures were isolated by FACS. Cells were stained with a distinct barcoded antibody (Cell Hashing antibody, TotalSeq-A, BioLegend) as described previously (20). Next, 7,000 cells from each condition were resuspended in 0.4% BSA in PBS at a concentration of 1,000 cells per μL, pooled together, then loaded onto a single lane (Chromium chip, 10× Genomics), followed by encapsulation in a lipid droplet (Single Cell 3′kit V3, 10× Genomics), followed by cDNA and library generation according to the manufacturer's protocol. For the scRNA-seq analysis of the parent tumor, 6,000 viable $CD45^+$ cells and 4,000 $CD45^-$ (tumor and stromal cells) were pooled together and resuspended in 0.4% BSA in PBS at a concentration of 1,000 cells per μL. A total of 10,000 cells were loaded onto a single lane (Chromium chip, 10× Genomics), followed by encapsulation in a lipid droplet (Single Cell 3′kit V3, 10× Genomics), followed by cDNA and library generation according to the manufacturer's protocol.

mRNA libraries were sequenced to an average of 50,000 reads per cell and HTO (Cell Hashing antibodies) libraries sequenced to an average of 5,000 reads per cell, both using Illumina Novaseq. Please see Supplementary Materials and Methods for scRNA-seq data analysis methods.

In vivo study

Massachusetts General Hospital Institutional Care and Use Committee protocol 2017N0000236 was used for this study. STOSE cells were cultured and expanded as described previously (21). Twenty 7–9 week-old FVB-N mice obtained from Jackson Labs were intraperitoneally injected with 1×10^7 STOSE cells in 250 μL of PBS. Eighteen days post-injection, mice were weighed and randomized into two arms (10/arm). Randomization was done so that the average weights, weight gained compared with day 0, and SDs were close between the two arms upon starting treatment. The mice were treated with either vehicle [10% NMP (Thermo Fisher Scientific, catalog no. 390682500), 90%PEG400 (Sigma, catalog no. 202398-500G)] or 150 mg/kg BAY-299 (MedChemExpress, HY-107424) by oral gavage once per day for 18 days. Animals were monitored by weight every 3 to

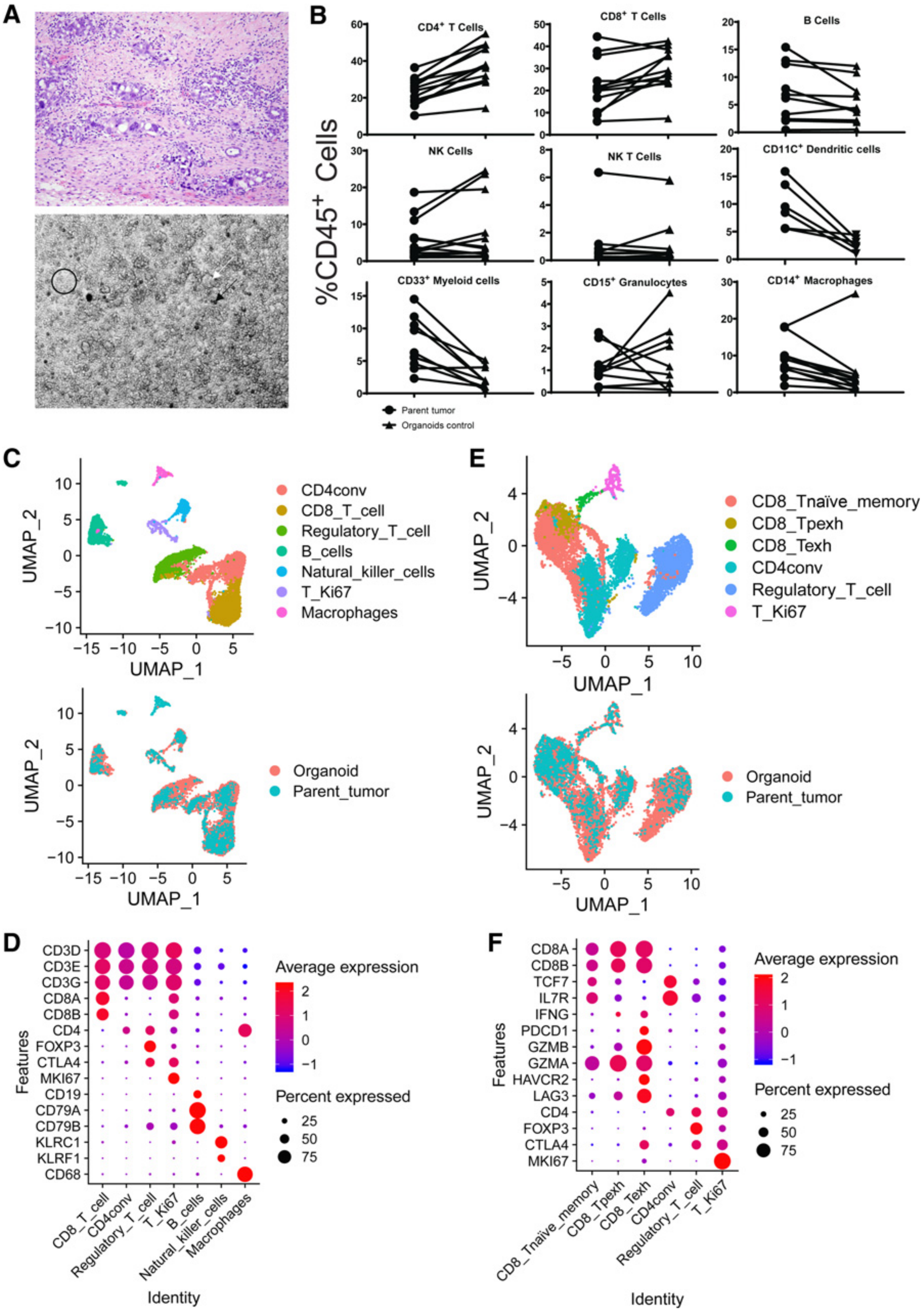
A
B
%CD45⁺ Cells
CD4⁺ T Cells
CD8⁺ T Cells
B Cells
NK Cells
NK T Cells
CD11C⁺ Dendritic cells
CD33⁺ Myeloid cells
CD15⁺ Granulocytes
CD14⁺ Macrophages
Parent tumor
Organoids control
C
UMAP_1
UMAP_2
CD4conv
CD8_T_cell
Regulatory_T_cell
B_cells
Natural_killer_cells
T_Ki67
Macrophages
Organoid
Parent_tumor
D
Features
CD3D
CD3E
CD3G
CD8A
CD8B
CD4
FOXP3
CTLA4
MKI67
CD19
CD79A
CD79B
KLRC1
KLRF1
CD68
Average expression
Percent expressed
25
50
75
Identity
E
CD8_Tnaïve_memory
CD8_Tpexh
CD8_Texh
CD4conv
Regulatory_T_cell
T_Ki67
F
CD8A
CD8B
TCF7
IL7R
IFNG
PDCD1
GZMB
GZMA
HAVCR2
LAG3
CD4
FOXP3
CTLA4
MKI67

4 days and dosing was adjusted by weight. At the end of the study, mice were euthanized, and ascites and tumors were harvested. Preparation of ascites and tumor cell suspensions for analysis is described in Supplementary Methods.

Accession number

The sequencing data discussed in this study have been deposited in NCBI's Gene Expression Omnibus (GEO) database and are accessible through GEO Series accession number GSE160755.

Results

HGSC organoid–immune cell co-cultures resemble the immune microenvironment of their parent tumors

Short-term co-cultures containing tumor organoids and the full complement of intratumoral immune cells were generated from solid tumors from 12 patients with HGSC, with two sites for 1 patient, making 13 total cultures (**Fig. 1**; Supplementary Fig. S1A). Co-cultures were maintained in a limited growth matrix with minimal growth factor enrichment of the media; experiments occurred immediately after surgery and only lasted 96 hours. These strategies help prevent confounding alterations to the microenvironment, which might occur in longer cultures such as clonal selection of T cells (22, 23). Co-cultures were validated as matching parent tumors through visual, flow cytometry, and sequencing methods.

Bright-field microscopy revealed the co-cultures "look" similar to their parent tumors and contain psammoma body calcifications and groups of tumor spheres permeated by sheets and clusters of immune cells (**Fig. 1A**). Flow cytometry analysis of the parent tumors revealed a significant population of T cells with CD4 cells comprising the majority in most cases, similar to other HGSC studies (24), and revealed a significant population of NK and NK T cells (Supplementary Figs. S1B, S1C and S2A). Flow cytometry comparison of the organoids and parent tumors revealed similar amounts of each immune cell type present in the co-cultures with overall proliferation of T and NK cells and an expected drop in myeloid cells over time (**Fig. 1B**; Supplementary Figs. S1C, S2A and S2B). Significant PD-1, PD-L1, and TIM3 expression was found on relevant immune populations and tumor cells in the co-cultures (Supplementary Figs. S3A–S3D, S4A–S4C and S5A–S5C).

scRNA-seq analysis comparing a single matched parent tumor and control-treated organoid co-culture (20-11) revealed similar annotation of all immune cell types (**Fig. 1C**) defined by standard immune markers (**Fig. 1D**) with a decrease in macrophages mirroring flow cytometry (**Fig. 1B**; Supplementary Fig. S1C). Standard T-cell subsets were detected (**Fig. 1E**) using common subset markers (**Fig. 1F**).

Overall, these flow cytometry and scRNA-seq results confirm that the organoid co-cultures authentically model the parent tumor immune microenvironment.

ICB antibodies reproducibly induce IFNγ production in co-cultures

We next tested the immune activation capacity of ICB antibodies in our system. We sought to compare the efficacy and mechanism of action of a novel bispecific anti-PD-1/PD-L1 antibody (LY3434172; ref. 19) to its monospecific controls, anti-PD-1 (pembrolizumab) and anti-PD-L1 (LY3300054; Supplementary Fig. S6A; ref. 25). Monospecific ICB antibody combinations demonstrate some clinical success (26), but bispecific antibodies are hypothesized to be more effective given their ability to engage two different ICB receptors in close proximity (19, 27). Indeed, compared with monospecific controls, the bispecific anti-PD-1/PD-L1 antibody (LY3434172) has been shown to increase T-cell stimulation in a different *in vitro* system and anti-tumor efficacy *in vivo* in humanized ovarian and other tumor xenograft mouse models through unclear mechanisms (19). On the basis of this, we hypothesized that studying the function of the bispecific anti-PD-1/PD-L1 antibody, compared with controls, in our co-culture system could help dissect critical targets not being affected by available monospecific ICB antibodies.

To measure overall immune response, we performed IFNγ ELISA analysis on media from the 13 co-cultures post-treatment with a physiologic dose of each of the four antibodies individually. Pilot ELISA studies indicated 96 hours post-treatment as the best timepoint (Supplementary Fig. S6B). In six cases, media containing anti-PD-1 and anti-PD-L1 combined or an equivalent amount of IgG (IgG+IgG) was tested to determine whether increased bispecific antibody efficacy was due to an additive effect.

For every tumor analyzed, all three ICB antibodies induced significantly increased IFNγ production compared with the isotype control (**Fig. 2A** and **B**; Supplementary Fig. S6C). The bispecific antibody induced the strongest IFNγ production, not attributable to an additive effect as evidenced by the lower IFNγ production for the anti-PD-1+anti-PD-L1 combination (**Fig. 2A**; Supplementary Fig. S6D).

To compare the aggregate immune activation state of the parent tumors and co-cultures, we generated *IFNG* expression signature scores for each parent tumor as a measure of the bulk tumor immune state, and compared the scores with the co-culture ELISA results as a measure of bulk organoid immune state (**Fig. 2B**; ref. 28). The co-cultures with the highest IFNγ ELISA signals derived from parent tumors with the highest *IFNG* scores (19-107, 19-109, 20-19 omentum), those with medium IFNγ ELISA signals were from parent

Figure 1.

HGSC organoid co-cultures accurately mimic the parent tumors from which they were derived. **A,** Organoid co-cultures (bottom) physically resemble the diverse cellular environment of the parent tumor (top), which includes cancer, stromal, and immune cells. The co-cultures contain tumor spheres (white arrow), clusters of single immune and stromal cells (black circle), and psammoma body calcifications (black arrow). **B,** Flow cytometry analysis for all immune cell types was performed on parent tumors and control-treated organoids. Comparisons of each individual immune cell type between parent tumor (circles) and control-treated organoid co-culture (triangles) as a percentage of viable CD45$^+$ cells are shown. **C–F,** scRNA-seq analysis results comparing the parent tumor and treated organoid co-cultures for patient 20-11. **C,** UMAPs are shown here to demonstrate concordance across all immune cell types between the parent tumor and organoid co-culture. All populations detected are shown on top with a color key on the right, and an overlay of these populations in the parent tumor (blue) and organoid co-cultures (orange) is shown below. **D,** Markers (*y*-axis) used to define each of the individual immune cell populations (*x*-axis) in **C** are shown here along with the expression level in each defined cell type. The average expression level (colors) is shown in the percentage of cells (sphere) expressing each marker for each cell type. **E,** UMAPs are shown here to demonstrate concordance across all T-cell types between the parent tumor and organoid co-culture. All populations detected are shown on top with a color key on the right, and an overlay of these populations in the parent tumor (blue) and organoid co-cultures (orange) is shown below. **F,** Markers (*y*-axis) used to define each of the different T-cell populations (*x*-axis) in **E** are shown here along with the expression level in each defined cell type. The average expression level (colors) is shown in the percentage of cells (sphere) expressing each marker for each cell type. CD8_Tnaïve_memory, naïve and memory CD8 T cells; CD4conv, conventional nonregulatory CD4 T cells; regulatory_T_cell, regulatory CD4 T cells; T_Ki67, proliferating T cells; CD8_Texh, terminally exhausted CD8 T cells; CD8_Tpexh, progenitor-exhausted CD8 T cells.

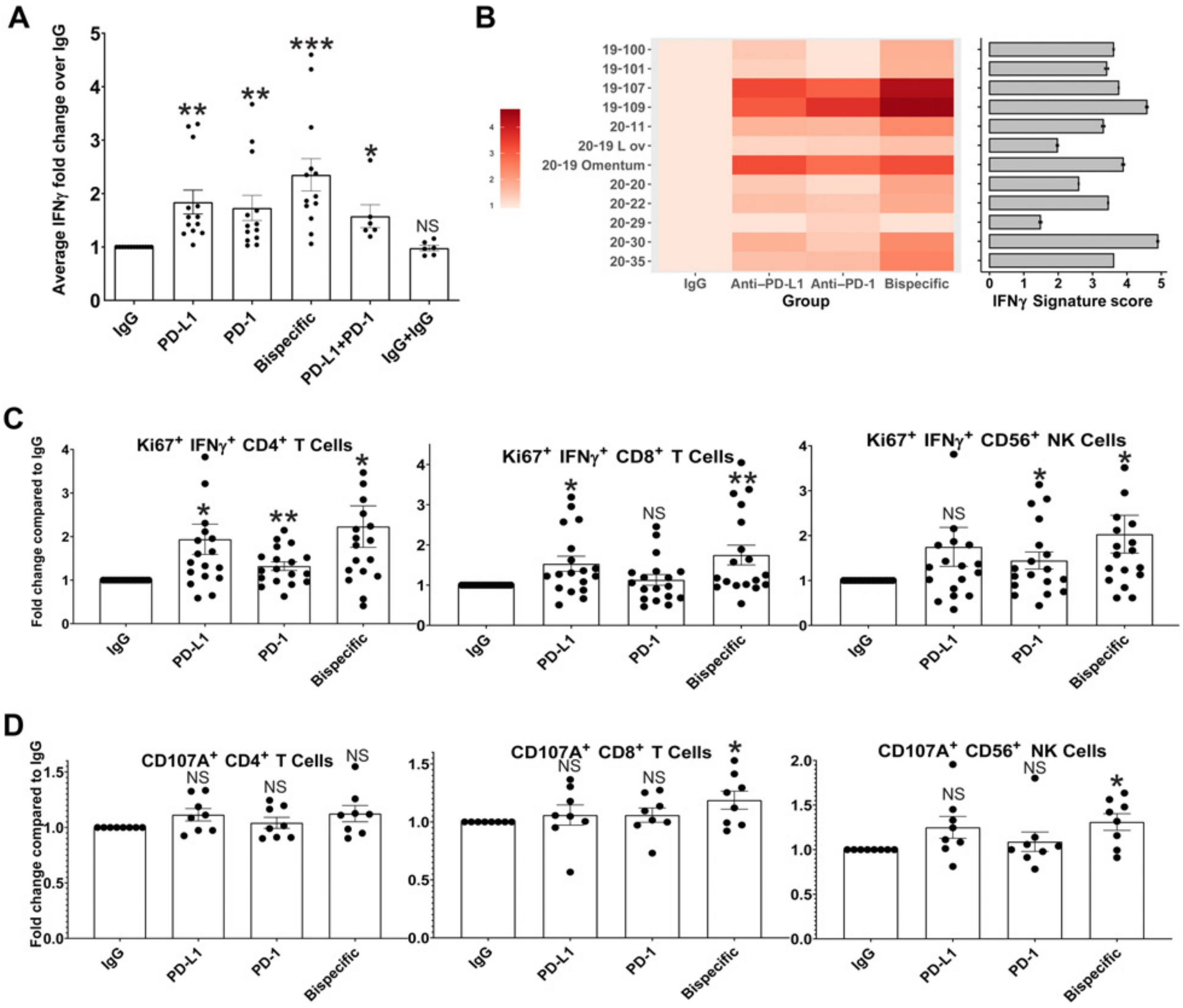

Figure 2.

ICB antibodies induce detectable IFNγ production in proportion to the parent tumor aggregate immune state, increased CD4, CD8, and NK-cell activity, and a killing phenotype in CD8 T and NK cells in HGSC co-cultures. **A,** IFNγ ELISA analysis was performed on media from organoid co-cultures treated with IgG control, anti-PD-L1, anti-PD-1, anti-PD-1/PD-L1 (bispecific), anti-PD-1+anti-PD-L1, and IgG+IgG. Average IFNγ amounts normalized to the IgG control are shown here across all experiments with error bars representing SEM. *P* values were calculated for all comparisons using a paired *t* test. Comparisons of key antibodies to the IgG control are shown. *, $P < 0.05$; **, $P < 0.005$; ***, $P < 0.0005$. *P* values for the significance of other treatment comparisons are shown in Supplementary Fig. S6. **B,** A heatmap is shown for the normalized ELISA results of each individual tumor for IgG, anti-PD-L1, anti-PD-1, and the bispecific antibody. The color code is shown on the left. In addition, bulk RNA-seq was performed on the parent tumors used to generate the co-cultures, and an *IFNG* signature score was generated. Each tumor was sequenced twice, and the average *IFNG* score from each parent tumor is shown to the right of the heatmap as a horizontal bar graph with the number score key below. Error bars, SD. **C,** Flow cytometry analysis for IFNγ/Ki67 double-positive CD4^{+}, CD8^{+}, and CD56^{+} NK cells across treatments normalized to the IgG control. **D,** Flow cytometry analysis for CD107A expression on CD4^{+}, CD8^{+}, and CD56^{+} NK cells across treatments normalized to the IgG control. *, $P < 0.05$; **, $P < 0.005$; NS, not significant. Error bars, SEM.

tumors with medium scores (19-100, 19-101, 20-11, 20-20, 20-22, and 20-35), and the cultures with low IFNγ ELISA signal derived from the lowest scoring parent tumors (20-29 and 20-19, left ovary; **Fig. 2B**). Patient 20-30 is an outlier with a parent tumor with a high *IFNG* score but co-cultures with a medium IFNγ signal by ELISA (**Fig. 2B**), potentially due to sampling discrepancies between tissue used for culture and sequencing. Overall, these results indicate that the parent tumor immune activation state is largely matched by the co-cultures and supports the hypothesis that the quality of the immune cells in a tumor rather than the quantity dictate ICB response.

Given our ability to detect immune responses in the co-cultures, we next asked which cells each antibody targets to induce this response.

Different ICB antibodies induce varying degrees of activation in unique immune cell types

Treated organoid co-cultures were analyzed by flow cytometry to determine which cell population(s) each antibody affected by searching for changes in cell numbers and activation markers.

Cell numbers for each lineage were unaffected by the antibodies. There were no changes in T- or NK-cell numbers, CD69^{+} active T-cell numbers, or the ratio of CD4:CD8 T cells across all treatments (Supplementary Fig. S7A–S7C). There were no changes in any myeloid cell type except for a small but statistically significant decrease in $CD14^+$ macrophages induced by the bispecific antibody compared with the isotype control (Supplementary Fig. S7A).

We assessed all cell types for markers of proliferation (Ki67), antigen stimulation (IFNγ), and cytotoxic phenotype [granzyme B (GZMB) and CD107A; **Fig. 2C** and **D**; Supplementary Fig. S8A–S8D]. All three ICB antibodies induced a statistically significant increase in antigen-stimulated proliferating Ki67/IFNγ double-positive CD4 and

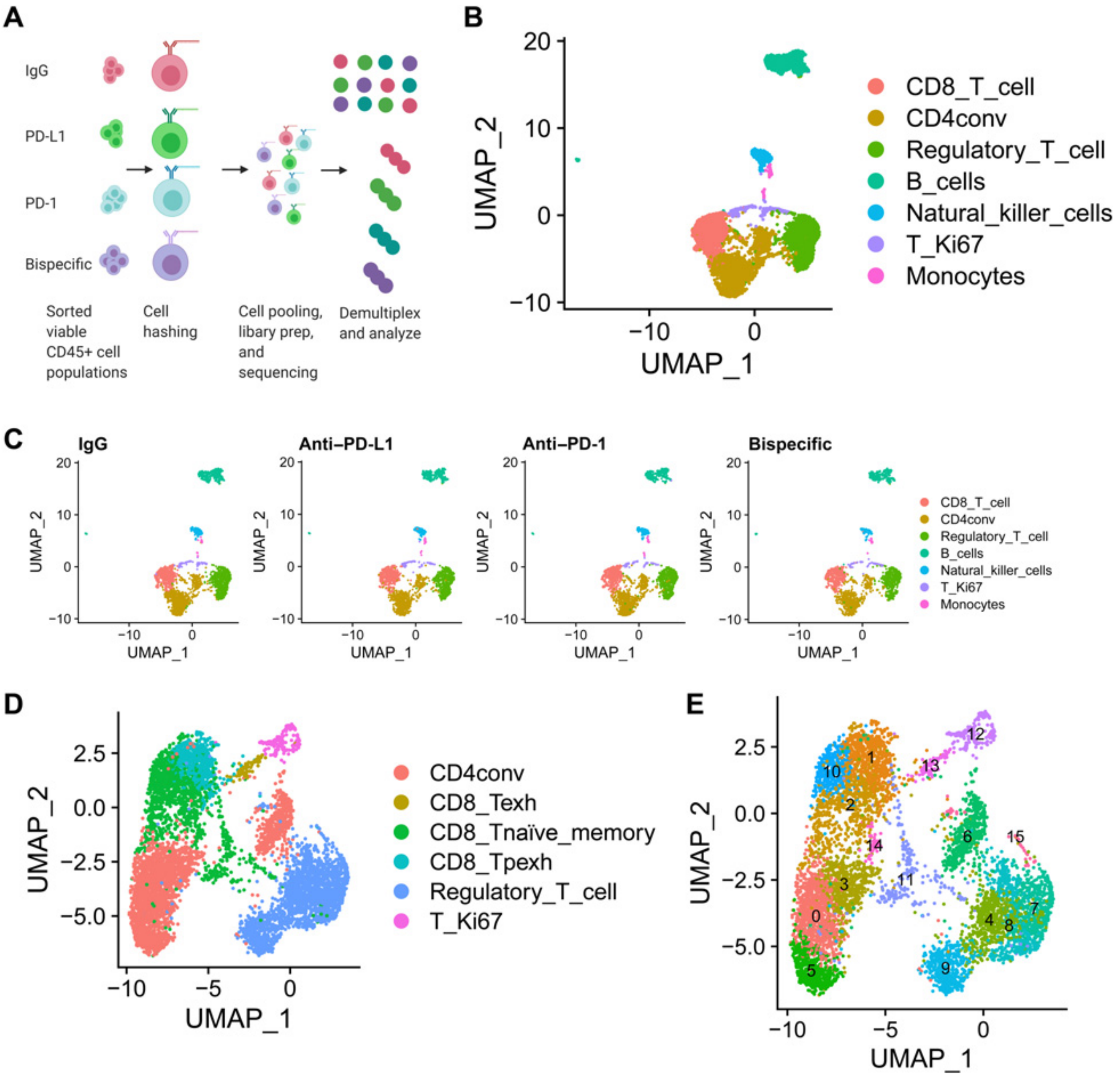

Figure 3.

scRNA-seq analysis of treated organoid co-cultures offers a comprehensive assessment of all immune cell types post-ICB treatment. **A,** Schematic of scRNA-seq experiment. A single organoid co-culture was treated with isotype control, anti-PD-L1, anti-PD-1, or anti-PD-1/PD-L1. Viable $CD45^+$ cells were sorted 96 hours later, hashed with different barcodes for each treatment, mixed in equal proportion, and submitted for 10× genomics library preparation and subsequent sequencing analysis. **B–E,** scRNA-seq analysis comparing results in the organoid co-cultures across treatments. **B,** UMAP demonstrating all immune cells detected in the pool of mixed cells from all treatments from the organoid co-cultures. The color code for each cell type is shown on the right. **C,** UMAPs demonstrating the cells detected in organoid co-cultures from each treatment in the populations in **B** are shown separately to demonstrate equal distribution of all lineages across treatment. Treatment is indicated above the graph and cell type is indicated by a color code on the right. **D** and **E,** UMAPs are shown to demonstrate all T-cell subsets detected across the mixture of cells analyzed across all four treatments and that within each of these subsets there are 15 separate clusters with unique transcriptional states. Cell types are indicated by color codes on the right, and clusters are numbered in **E**. CD4conv, conventional nonregulatory CD4 T cells; T_Ki67, proliferating T cells; CD8_Tpexh, progenitor-exhausted CD8 T cells; CD8_Tnaïve_memory, naïve and memory CD8 T cells; regulatory_T_cell, regulatory CD4 T cells; CD8_Texh, terminally exhausted CD8 T cells.

CD8 T cells and NK cells, with the bispecific antibody induction the strongest for all three cell types (**Fig. 2C**). Only the bispecific antibody induced an increased percentage of CD107A$^+$ CD8 T cells and NK cells over the IgG control (**Fig. 2D**). Finally, the bispecific antibody induced a small but discernible increase in GZMB-positive CD4 and CD8 T cells and NK cells (Supplementary Fig. S8D). Taken together with the ELISA results, these data indicate that the bispecific antibody induces both an increase in T- and NK-cell activation and cytotoxicity more efficiently than the controls. To better understand the mechanism of ICB antibody-driven immune activation in these cell types, we performed scRNA-seq analysis.

scRNA-seq of treated organoid co-cultures reveals differential expression in all immune lineages after multiple treatment modalities

To study the effects of each ICB antibody on every kind of immune cell in a tumor, we performed scRNA-seq analysis on organoid co-cultures from an untreated HGSC omental metastasis (20-11) 96 hours

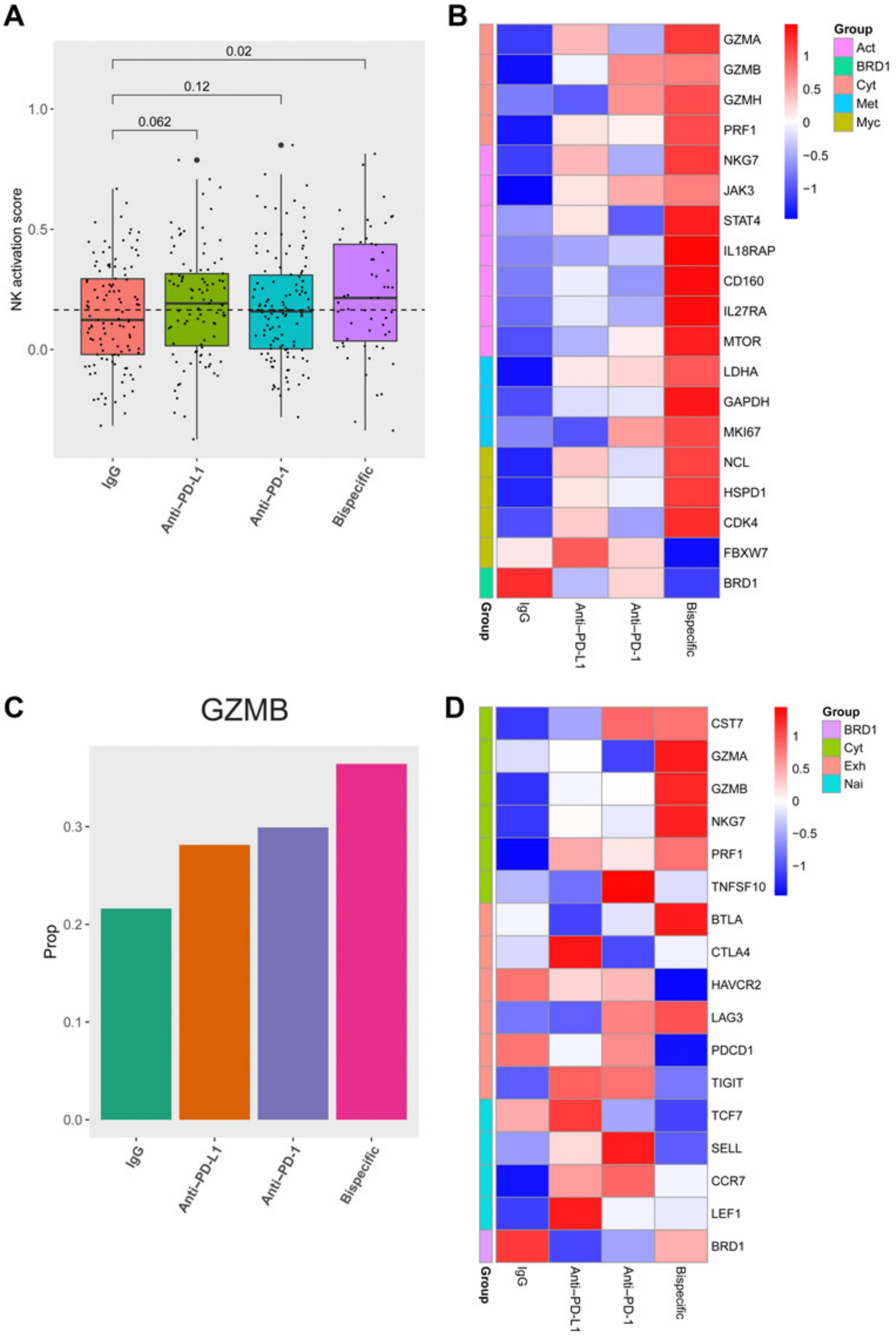

Figure 4.

scRNA-seq analysis reveals that the bispecific antibody induces an increased cytotoxic phenotype in CD8 T cells and NK cells and a decreased exhaustion and naivety phenotype in CD8 T cells. **A,** Activation scores were generated by assessing a panel of 22 genes associated with NK-cell activation. Box plots of the average scores for each treatment are shown, with *P* values on top generated using a one-tailed *t* test compared with the isotype control. **B,** A heatmap demonstrating Z scores generated from mean expression in NK cells for genes related to cytotoxicity (cyt; top), activation (act; second from top), metabolism (met; second from bottom), Myc signaling (Myc; third from bottom), and BRD1 (bottom) is shown comparing IgG, anti-PD-L1, anti-PD-1, and the bispecific antibody. **C,** The positive rate of GZMB expression across all treatments in all CD8 T-cell populations combined is shown. **D,** A heatmap demonstrating Z scores generated from mean expression in all CD8 T-cell populations combined for genes related to cytotoxicity (cyt; top), exhaustion (exh; second from top), naivety (nai; second from bottom), and BRD1 (bottom) is shown comparing IgG, anti-PD-L1, anti-PD-1, and the bispecific antibody.

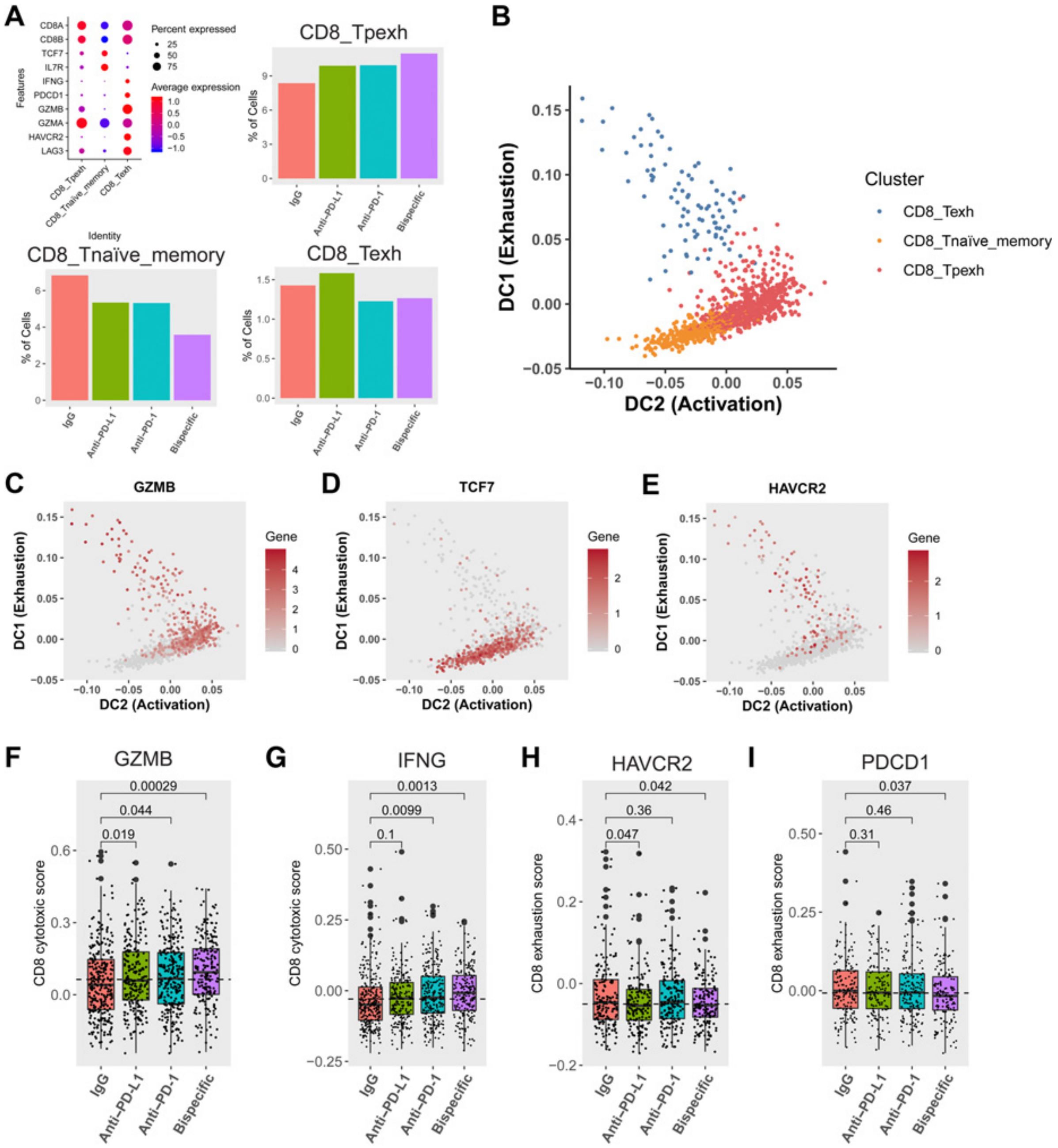

Figure 5.

scRNA-seq analysis reveals state changes in CD8 T cells between distinct subsets. **A,** Definition of and percentage of CD8 T cells in naïve (CD8_Tnaive_memory), progenitor-exhausted (CD8_Tpexh), and terminally exhausted (CD8_Texh) CD8 T-cell groups (mapped in **Fig. 3D** and **E**). On the top left is a bubble map demonstrating markers used to define these three groups. Markers (*y*-axis) used to define each of the different groups (*x*-axis) are shown here along with the expression level in each defined cell type. The average expression level (colors) is shown in the percentage of cells (sphere) expressing each marker for each cell type. Bar graphs demonstrating the proportion of CD8 T cells in progenitor-exhausted (top right), naïve (bottom left), and terminally exhausted (bottom right) CD8 T-cell groups across antibody treatments are shown. **B,** Diffusion map demonstrating transition between (i) naïve (orange) and progenitor-exhausted (red) cells, and (ii) terminally exhausted (blue) and progenitor-exhausted (red) cells over pseudotime. The *x*-axis represents increasing activation, and the *y*-axis represents increasing exhaustion. The color code for the different clusters/subgroups is shown on the top right. **C–E,** Diffusion maps demonstrating transition between naïve and progenitor-exhausted cells and terminally exhausted and progenitor-exhausted cells (mapped in **B**) over pseudotime for the activation marker *GZMB* (**C**), the naivety marker *TCF7* (**D**), and the exhaustion marker *HAVCR2* (TIM3; **E**). The *x*-axis represents increasing activation, and the *y*-axis represents increasing exhaustion. The color code for gene expression level is shown on the right. **F** and **G,** Activation scores were generated by assessing a panel of 50 genes associated with *GZMB* (**F**) or *IFNG* expression (**G**) in CD8 T cells in naïve and progenitor-exhausted CD8 T cells. Box plots of the average scores for each treatment are shown with *P* values compared with the IgG control for *GZMB* (**F**) and *IFNG* (**G**). **H** and **I,** Exhaustion scores were generated by assessing a panel of 50 genes associated with *HAVCR2* (TIM3; **H**) expression or *PDCD1* (PD-1; **I**) expression in CD8 T cells in both naïve and progenitor-exhausted cells. Box plots of the average scores for each treatment are shown with *P* values compared with the control for *HAVCR2* (**H**) and *PDCD1* (**I**). All *P* values were generated using a one-tailed *t* test.

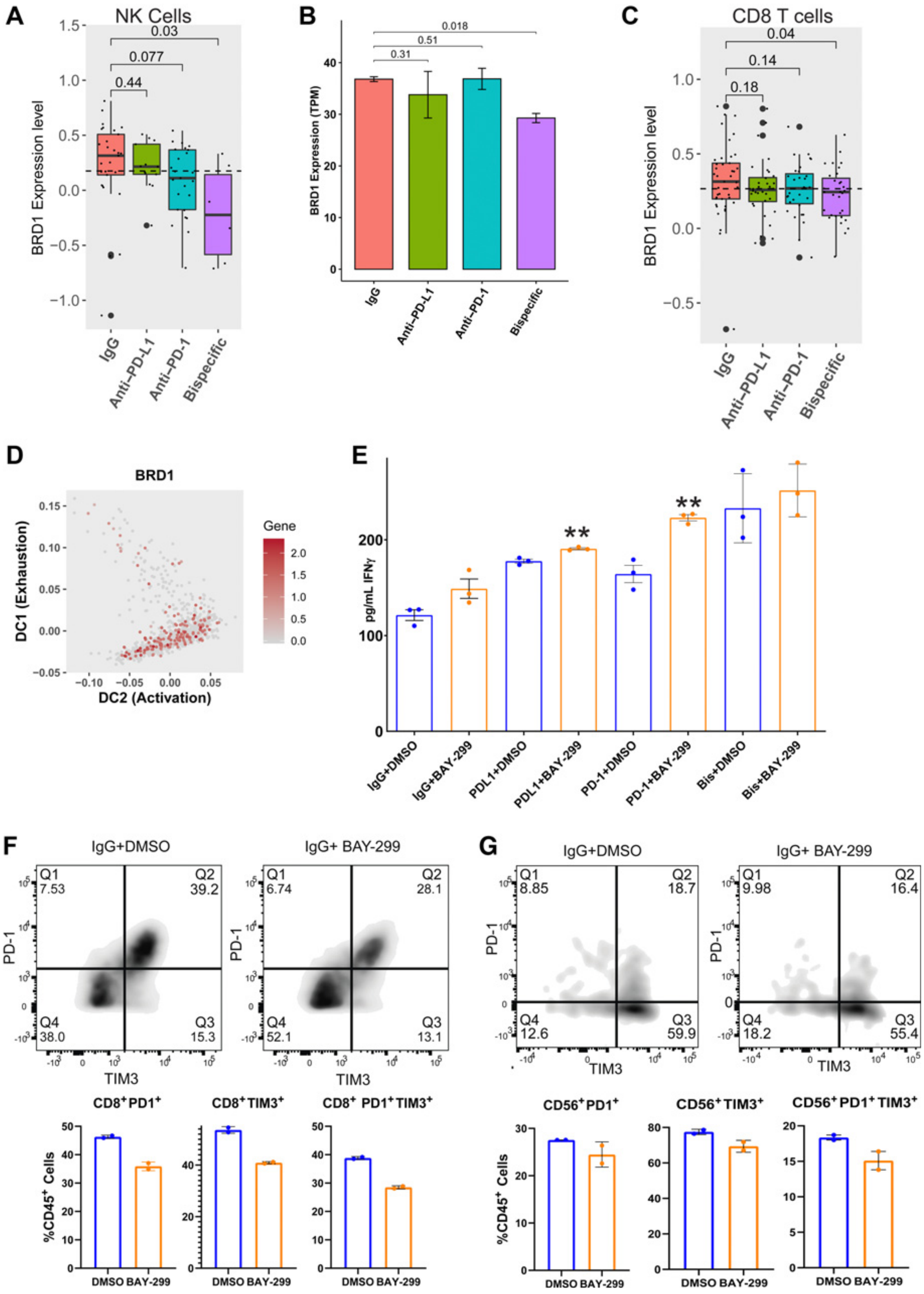
A
NK Cells
BRD1 Expression level
1.5
1.0
0.5
0.0
−0.5
−1.0
0.03
0.077
0.44
IgG
Anti–PD-L1
Anti–PD-1
Bispecific
B
BRD1 Expression (TPM)
0.018
0.51
0.31
40
30
20
10
0
IgG
Anti–PD-L1
Anti–PD-1
Bispecific
C
CD8 T cells
BRD1 Expression level
0.04
0.14
0.18
1.0
0.5
0.0
−0.5
IgG
Anti–PD-L1
Anti–PD-1
Bispecific
D
BRD1
DC1 (Exhaustion)
0.15
0.10
0.05
0.00
−0.05
DC2 (Activation)
−0.10
−0.05
0.00
0.05
Gene
2.0
1.5
1.0
0.5
0.0
E
pg/mL IFNγ
200
100
0
**
**
IgG+DMSO
IgG+BAY-299
PDL1+DMSO
PDL1+BAY-299
PD-1+DMSO
PD-1+BAY-299
Bis+DMSO
Bis+BAY-299
F
IgG+DMSO
IgG+ BAY-299
PD-1
TIM3
Q1 7.53
Q2 39.2
Q4 38.0
Q3 15.3
Q1 6.74
Q2 28.1
Q4 52.1
Q3 13.1
CD8⁺PD1⁺
CD8⁺TIM3⁺
CD8⁺ PD1⁺TIM3⁺
%CD45⁺ Cells
DMSO
BAY-299
G
IgG+DMSO
IgG+ BAY-299
PD-1
TIM3
Q1 8.85
Q2 18.7
Q4 12.6
Q3 59.9
Q1 9.98
Q2 16.4
Q4 18.2
Q3 55.4
CD56⁺PD1⁺
CD56⁺TIM3⁺
CD56⁺PD1⁺TIM3⁺
%CD45⁺ Cells
DMSO
BAY-299

post-treatment, with isotype control, anti-PD-1, anti-PD-L1, or the bispecific antibody (**Fig. 3A**). Viable CD45$^+$ cells from each treatment were sorted, hashed (20), harvested for library preparation, and sequenced (**Fig. 3A**).

Analysis and cell type annotation of the pooled samples revealed every immune cell type was detectable (**Fig. 3B**) with equal numbers of each immune cell type present across all four treatment groups (**Fig. 3C**). All T-cell subtypes were present (**Fig. 3D**), and unsupervised clustering by Seurat (29) identified 15 unique T-cell subsets/clusters each with distinct transcriptional states (**Fig. 3E**). All immune cell types showed differential expression across treatments (Supplementary Figs. S9A–S9N, S10A–S10D and S11A–S11K; Supplementary Tables S1–S4).

Gene expression analysis reveals increased cytotoxicity in T and NK cells and decreased exhaustion in T cells induced most strongly by the bispecific antibody

We analyzed CD8 T and NK cells for activity or cytotoxicity marker expression. For NK cells, we analyzed expression across a panel of 22 NK-cell activation genes to generate activation scores for each treatment (**Fig. 4A**; Supplementary Table S5; ref. 30). The highest and only statistically significant score was for the bispecific antibody compared with the isotype control. Furthermore, we analyzed expression of genes associated with NK-cell cytotoxicity, activation, metabolism, and Myc signaling (30–33). Upregulation of c-Myc or its targets and downregulation of Myc degraders (FBXW7) cause NK-cell expansion and metabolic activation (32, 34). The bispecific antibody induced the greatest increase in expression of all cytotoxicity, activation, metabolism, and Myc targets and the strongest decrease of *FBXW7* (**Fig. 4B**). Bispecific antibody upregulation of *GZMB* was independently verified in sorted NK cells from a different patient's treated organoid co-cultures (Supplementary Fig. S10D). These results suggest a state change from inert to highly active. Neither monospecific antibody induced NK-cell activation, suggesting that NK-cell activation is a unique bispecific antibody target.

Gene expression analysis of bulk CD8 T cells revealed that all ICB agents induced *GZMB* expression, most strongly the bispecific antibody (**Fig. 4C**), validating flow cytometry findings (Supplementary Fig. S8D). The bispecific antibody induced a larger increase in expression of multiple cytotoxicity markers, including *GZMA, GZMB*, and *PRF1* (**Fig. 4D**). *GZMB* upregulation was validated in CD8 T cells sorted from organoid co-cultures from a different patient (Supplementary Fig. S11G). In addition, the bispecific antibody induced an overall decrease in expression of a subset of exhaustion markers (*PDCD1* = PD-1 and *HAVCR2* = TIM3) and naïve T-cell markers (*TCF7* and *SELL*), suggesting a shift of the CD8 T cells from naïve and exhausted states to active (**Fig. 4D**). However, shifts in the bulk CD8 T-cell analysis were small and sometimes inconsistent across functional groups (**Fig. 4D**). In other tumor types, small subsets of CD8 T cells respond to ICB therapies (10, 11), prompting us to reexamine activation and exhaustion marker expression in each CD8 subset to determine the reason for the smaller shifts we were observing in the bulk CD8 T-cell analysis and if this also occurs in HGSC (**Fig. 4C** and **D**).

CD8 T-cell trajectory analysis suggests a state transition induced by ICB antibodies

To identify which CD8 T cells respond to ICB agents, we focused on three subsets including naïve, progenitor exhausted, and terminally exhausted, all defined by varying expression of activation, naivety, and exhaustion markers (**Fig. 5A**; refs. 10, 11). Examination of these subsets across the four treatment groups reveals (i) an increase in progenitor exhausted and a decrease in naïve groups both most prominent after bispecific antibody treatment, and (ii) small decreases within the terminally exhausted group after anti-PD-1 and bispecific antibody treatment (**Fig. 5A**). This suggested a state transition within these groups in response to ICB (10, 11).

To define the direction of the dynamic state shifts between these three CD8 T-cell groups in response to treatment, we utilized diffusion maps of activation (*GZMB, PRF1, IFNG*), naivety (*TCF7, SELL*), and exhaustion [*HAVCR2* (TIM3)] markers ordered in pseudotime (**Fig. 5B–E**; Supplementary Fig. S11H–S11J; refs. 11, 35). The activation markers increase between naive and progenitor exhausted, and terminally exhausted and progenitor-exhausted cells (**Fig. 5B**; Supplementary Fig. S11H and S11J), the naivety markers decrease from naïve into progenitor-exhausted cells (**Fig. 5D**; Supplementary Fig. S11I), and the exhaustion markers decrease from terminally exhausted into progenitor-exhausted cells and from progenitor exhausted into naïve cells (**Fig. 5E**). These transitions are most significantly induced by the bispecific antibody (**Fig. 5A**). Overall, this suggests that naïve CD8 T cells might give rise to the progenitor-exhausted active subset, and that some terminally exhausted cells shift

Figure 6.

The bispecific antibody acts, in part, through strongly depleting *BRD1* expression, leading to increased immune activity through activation and state changes in T and NK cells. **A,** *BRD1* expression was analyzed across different treatment groups from the scRNA-seq experiment (**Fig. 3**) for NK cells. Bar graph demonstrating the expression level of *BRD1* in NK cells for each ICB antibody compared with the IgG control. *P* values were generated using a one-tailed *t* test. **B,** To verify the *BRD1* depletion induced by the bispecific antibody in NK cells, another organoid co-culture from an untreated patient with HGSC (20–35) was treated with isotype control, anti-PD-1, anti-PD-L1, or anti-PD-1/PD-L1. NK cells were sorted from the treated cultures at the 96-hour timepoint and sent for bulk RNA-seq. The *BRD1* expression across treatments is shown here as transcripts per million (TPM). *P* values were generated using a one-tailed *t* test. **C,** *BRD1* expression was analyzed across different treatment groups from the scRNA-seq experiment (**Fig. 3**) for the naïve and progenitor-exhausted CD8 T-cell subgroups combined. Shown here is a bar graph demonstrating the expression level of *BRD1* in the combined ICB-responsive naïve and progenitor-exhausted CD8 T cells compared with the IgG control. *P* values were generated using a one-tailed *t* test. **D,** Diffusion map demonstrating *BRD1* expression in CD8 T-cell subgroups transitioning between naïve and progenitor-exhausted CD8s and terminally exhausted and progenitor-exhausted CD8s (mapped in **Fig. 5B**). The *x*-axis represents increasing activation, and the *y*-axis represents increasing exhaustion. The color code for gene expression level is shown on the right. **E,** The same organoid co-culture from **B** (20–35) was treated with isotype control, anti-PD-1, anti-PD-L1, or anti-PD-1/PD-L1 combined with either DMSO (blue) or the BRD1 inhibitor BAY-299 (orange). The co-culture media supernatants underwent IFNγ ELISA analysis, shown here as the average pg/mL of IFNγ for the treatment, with error bars representing SE. **, $P < 0.005$. **F** and **G,** The treated organoid co-cultures from **B** and **E** underwent flow cytometry analysis for PD-1 and TIM3 single-positive and double-positive cells. Only the IgG and PD-L1–treated cultures could be analyzed here because the anti-PD-1 and bispecific antibody–treated co-cultures showed decreased PD-1 due to the treatment antibody blocking the flow antibody. **F,** The flow quadrant plots for IgG+DMSO and IgG+BAY-299 are shown for CD8 T cells on the top. PD-1 is on the *y*-axis and TIM3 is on the *x*-axis. The percentage of PD-1 (Q1) and TIM3 (Q3) single-positive and double-positive (Q2) CD8 T cells is shown on the bottom as a percent of CD45$^+$ cells. Error bars, SE across two replicates. **G,** The flow quadrant plots for IgG+DMSO and IgG+BAY-299 are shown for NK cells on the top. PD-1 is on the *y*-axis and TIM3 is on the *x*-axis. The percentage of PD-1 (Q1) and TIM3 (Q3) single-positive and double-positive (Q2) NK cells is shown on the bottom as a percent of CD45$^+$ cells. Error bars, SE across two replicates.

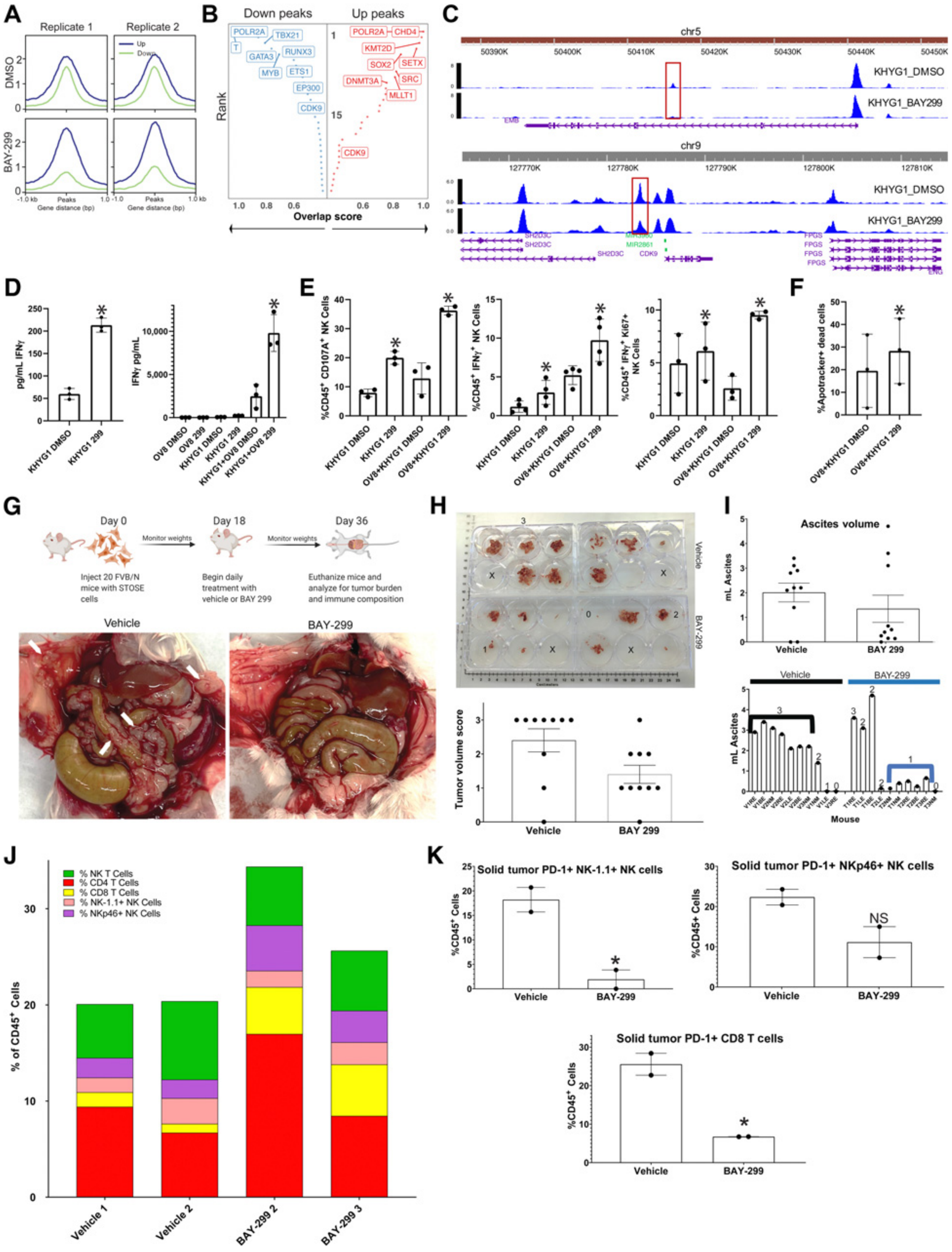
A
Replicate 1
Replicate 2
Up
Down
DMSO
BAY-299
Peaks
Gene distance (bp)
B
Down peaks
Up peaks
Rank
POLR2A
TBX21
T
RUNX3
GATA3
MYB
ETS1
EP300
CDK9
CHD4
KMT2D
SOX2
SETX
SRC
DNMT3A
MLLT1
Overlap score
C
chr5
KHYG1_DMSO
KHYG1_BAY299
EMB
chr9
SH2D3C
MIR2861
CDK9
FPGS
ENG
D
pg/mL IFNγ
IFNγ pg/mL
KHYG1 DMSO
KHYG1 299
OV8 DMSO
OV8 299
KHYG1+OV8 DMSO
KHYG1+OV8 299
E
%CD45⁺ CD107A⁺ NK Cells
%CD45⁺ IFNγ⁺ NK Cells
%CD45⁺ IFNγ⁺ Ki67⁺ NK Cells
OV8+KHYG1 DMSO
OV8+KHYG1 299
F
%Apotracker+ dead cells
G
Day 0
Day 18
Day 36
Monitor weights
Inject 20 FVB/N mice with STOSE cells
Begin daily treatment with vehicle or BAY 299
Euthanize mice and analyze for tumor burden and immune composition
Vehicle
BAY-299
H
Vehicle
BAY-299
Tumor volume score
Vehicle
BAY 299
I
Ascites volume
mL Ascites
Vehicle
BAY 299
Mouse
J
% NK T Cells
% CD4 T Cells
% CD8 T Cells
% NK-1.1+ NK Cells
% NKp46+ NK Cells
% of CD45⁺ Cells
Vehicle 1
Vehicle 2
BAY-299 2
BAY-299 3
K
Solid tumor PD-1+ NK-1.1+ NK cells
Solid tumor PD-1+ NKp46+ NK cells
Solid tumor PD-1+ CD8 T cells
%CD45⁺ Cells
NS
Vehicle
BAY-299

to the more active progenitor-exhausted state (**Fig. 5B**), both changes observed in other tumor types in response to ICB (10, 11).

Having defined the naïve and progenitor-exhausted groups as the ICB responders, we reexamined the exhaustion and activation marker gene panels, which revealed only small shifts in the bulk CD8 T cells (**Fig. 4D**). By assessing expression of the top 50 genes associated with either *GZMB* (**Fig. 5F**) or *IFNG* (**Fig. 5G**) in the combined progenitor-exhausted and naïve CD8 T-cell groups, we generated activation scores for these cells across treatments and found the largest statistically significant increases were for the bispecific antibody over the isotype control for both *GZMB* and *IFNG* (**Fig. 5F** and **G**). Similarly, we assessed expression across the top 50 genes associated with either *HAVCR2* (TIM3; **Fig. 5H**) or *PDCD1* (PD-1; **Fig. 5I**) in the same combined CD8 groups to generate exhaustion scores across treatments. We found a statistically significant decrease for anti-PD-L1 and the bispecific antibody over the isotype control for *HAVCR2*-associated genes (**Fig. 5H**) and for the bispecific antibody for *PDCD1*-associated genes (**Fig. 5I**). These results validated our findings regarding the decreased exhaustion and overall active state changes the bispecific antibody in particular induced within these CD8 groups (**Fig. 5B**).

We next sought to determine the mechanism of how the bispecific and other ICB antibodies induce these changes.

The bispecific antibody induces decreased T- and NK-cell exhaustion by downregulating BRD1 expression in immune cells

We examined the differentially expressed genes for the bispecific antibody compared with the controls in the CD8 T- and NK-cell populations, searching for cell state control genes with small-molecule therapies. We focused on the bromodomain-containing protein BRD1, which is known to regulate CD8 T and other cell development (36, 37) and has a small-molecule inhibitor, BAY-299 (38). *BRD1* expression was downregulated by the bispecific antibody in NK cells in the scRNA-seq data (**Figs. 4B** and **6A**; Supplementary Fig. S10A; Supplementary Table S4) and in bulk RNA seq of sorted NK cells from treated organoid co-cultures from a different patient (**Fig. 6B**). All ICB antibodies induced a decrease in *BRD1* expression in bulk (**Fig. 4D**) and combined ICB-responding progenitor-exhausted and naïve CD8 T cells (**Fig. 6C**), and by anti-PD-L1 in terminally exhausted CD8 T cells (Supplementary Fig. S11K). In diffusion analysis over pseudotime, *BRD1* expression decreased from naïve into progenitor exhausted cells and progenitor into terminally exhausted cells (**Fig. 6D**), suggesting the depletion was leading to an increase in activation and decrease in exhaustion. On the basis of these data, we hypothesized that BRD1 may negatively regulate T and NK cells and that BRD1 downregulation or inhibition may lead to enhanced antitumor immune function.

We examined *BRD1* expression in Tumor Immune Estimation Resource, a compilation of expression profiling of immune cells across multiple tumor types to determine whether *BRD1* expression in HGSCs *in vivo* correlates with immune cell inhibition (39). We found that *BRD1* expression is low in tumor cells and high in immune cells in HGSC (Supplementary Fig. S12). High *BRD1* expression correlated with significant downregulation of T- and NK-cell activity markers (*GZMA, GZMB, IFNG*, and *NKG7*) and upregulation of the naïve T-cell marker *TCF7* supporting our hypothesis that BRD1 is a negative regulator of T- and NK-cell activity (Supplementary Fig. S12).

To confirm that *BRD1* is a negative immune regulatory gene, we tested the BRD1 inhibitor BAY-299 (38) in HGSC organoid co-cultures. We observed that BAY-299 combined with isotype control, anti-PD-1, or anti-PD-L1 leads to a statistically significant increase in IFNγ levels over any antibody alone, indicating increased immune activation (**Fig. 6E**). BAY-299 addition generated only a small increase in IFNγ levels over bispecific antibody alone (**Fig. 6E**), as expected, given the bispecific antibody-induced depletion of BRD1 in key cell types (**Fig. 6A–C**).

Given the state transitions induced by the bispecific antibody (**Figs. 4** and **5**), we wondered whether BRD1 inhibition caused

Figure 7.

A BRD1 inhibitor causes increased anti-tumor immunity in HGSC by altering immune cell chromatin state. **A,** ATAC-seq was performed in duplicate on KHYG1 cells treated with either vehicle or BAY-299. Aggregated reads within 1 kb on either side of center for up (blue) and down (green) differentially accessible chromatin sites for the two replicates for DMSO (top) and BAY-299 (bottom)-treated cells are shown here. **B,** The transcription factors associated with the most strongly altered up (right; red) and down (left; blue) peaks are shown here. The *y*-axis represents rank of the transcription factor from 1 (highest rank at top) to 30 (lowest rank at bottom) for number of overlapping sites, and the *x*-axis represents the overlap score increasing from left to right for up peaks and right to left for down peaks. Highest ranking TFs are on the top left for down peaks and top right for up peaks. **C,** Chromatin peaks surrounding and within the *EMB* (top) and *CDK9* (bottom) genomic locus for DMSO-treated KHYG1 cells (top in each panel) and BAY-299–treated KHYG1 cells (bottom in each panel). The taller the peak, the more open the chromatin. The scale for peak size is on the *y*-axis and the *x*-axis represents location in the genome. **D,** KHYG1 cells treated with DMSO vehicle or BAY-299 (299) were plated either alone or in co-culture with OVCAR8 (OV8) tumor cells, and the media was subsequently tested for IFNγ presence by ELISA. Bar graphs for the ELISA for KHYG1 cells alone is shown on the left and for the co-cultures on the right. Error bars, SD between three replicates of the experiment. *, $P < 0.05$ using a paired *t* test. **E,** KHYG1 cells treated with vehicle DMSO or BAY-299 (299) were plated either alone or in co-culture with OVCAR8 (OV8) tumor cells, and the cultures were analyzed by flow cytometry for NK cell CD107A expression (left), IFNγ expression (middle), and IFNγ/Ki67coexpression (right). Error bars, SD between 3–4 replicates. *, $P < 0.05$ using a paired *t* test. **F,** KHYG1 cells treated with DMSO vehicle or BAY-299 (299) were plated in co-culture with OVCAR8 (OV8) tumor cells, and 6 hours later the OVCAR8 cells were analyzed for apoptotic death. The percentage of nonviable apoptotic cells (Apotracker+ Dead Cells) from three separate experiments is shown here for each group, with error bars representing SD. *, $P < 0.05$ using a paired *t* test. **G,** Top, a schematic of the *in vivo* experiment is shown. Bottom, gross images of the tumor burden in vehicle and BAY-299–treated mice are shown with white arrows pointing to solid tumor deposits on the peritoneum and bowel. The animals shown are representative of the most common tumor burden levels in each group. **H,** Top, grossly visible solid tumors were dissected from each mouse in each group, and a photo of tumor volume is shown. Solid tumors from each animal were placed in a well of a 6-well plate for visual volume scoring. A 3 represents high tumor burden; 2, medium tumor burden; 1, limited tumor burden; 0, no tumor burden. Numbers are placed in representative 3, 2, 1, and 0 wells, and an X is placed in empty wells. Bottom, the tumor volume scores are shown for all 10 animals per group in a bar graph, with error bars representing SEM. **I,** Ascites was aspirated from each animal and the volume measured. Top, a bar graph of the ascites volumes for all animals in each group, with the error bars representing SEM. Bottom, the individual animal ascites volumes with the numeric tumor volume score for each animal over the volume bar. Black and blue lines mark the vehicle and treatment groups most common volume and tumor burdens. **J,** Solid tumors were harvested from each animal in both the vehicle and treatment groups. For each treatment group, the tumors for 3–4 animals were combined. There were only enough cells from two combined groups each for vehicle and BAY-299 to perform flow analysis. The single-cell suspensions of the solid tumors were analyzed for T and NK composition, which is shown here. Each color represents a cell type and each bar represents a group. The color code is at the top left. **K,** PD-1 expression was analyzed in both solid tumor treatment groups on NK-1.1$^+$ NK cells (top left), NKp46$^+$ NK cells (top right), and CD8 T cells (bottom), and the percent of PD-1+ T or NK cells for each treatment group is shown here as a percentage of CD45$^+$ cells. Error bars, SD. *, $P < 0.05$ generated using an unpaired *t* test; NS, not significant with an unpaired *t* test.

increased immune efficacy through a cell state change. We examined exhaustion markers TIM3 and PD-1 (40) on T- and NK-cell populations from HGSC organoid co-cultures treated with our ICB antibody panel ± BAY-299 by flow cytometry. BAY-299 treatment decreased the number of TIM3 or PD-1 single-positive and TIM3/PD-1 double-positive CD3, CD4, and CD8 T cells and NK cells (**Fig. 6F** and **G**; Supplementary Fig. S13A and S13B), indicating that BRD1 inhibition may indeed be leading to a cell state change from an exhausted to an active phenotype as observed for all ICB antibodies, most significantly the bispecific antibody (**Figs. 4–6**). Thus, an underlying mechanism of action for the increased efficacy of the bispecific antibody is potentially an induction of *BRD1* depletion in NK and T cells, promoting active states (**Figs. 5** and **6**). The next question was how BRD1 depletion induces this state change and if it increases tumor cell killing.

BRD1 inhibition leads to increased NK-cell activation and tumor cell killing partially through altering chromatin access for key immune transcription factors

To study the mechanism of BRD1 inhibition–induced immune cell state changes, we applied BAY-299 to an NK-cell line, KHYG1 (41). BAY-299 caused a small decrease in BRD1 protein levels in the KHYG1 cells after a 96-hour exposure (Supplementary Fig. S14A). In a growth rate–corrected sensitivity analysis, BAY-299 was not overtly toxic to HGSC tumor, NK-, or T-cell or HGSC organoid lines (Supplementary Fig. S14B; ref. 42).

Assay for transposase-accessible chromatin using sequencing (ATAC-seq) analysis of BAY-299–treated KHYG1 cells revealed significant alterations to chromatin accessibility across the genome (**Fig. 7A**; Supplementary Fig. S14C). The major chromatin alterations showed significant overlap with binding sites for key NK-cell development regulatory transcription factors such as GATA3, TBX21, and TBXT, which were all associated with down peaks (**Fig. 7B**; ref. 43). Several genes linked to these transcription factors with important biological functions were in altered peaks. For example, BAY-299 caused alterations in the chromatin accessibility of the promoter region of *CDK9* (**Fig. 7C**, bottom). CDK9 is, in part, recruited to immune genomic loci by TBX21 as part of the PTef-b complex (44), and CDK9 inhibition allows global reactivation of epigenetically silenced genes, leading to increased IFNγ activity and sensitivity to ICB agents in tumor cells (45). In addition, BAY-299 reduces chromatin accessibility of *EMB* (**Fig. 7C**, top), another TBX21-regulated gene recently identified as a marker of immature NK cells and as part of an immature NK-cell signature (46). Taken together, these findings suggest that a possible BRD1 inhibitor mechanism of action is altering chromatin accessibility for major NK-cell regulatory transcription factors at key immune modulatory genes to allow for a mature (*EMB*) active and cytotoxic (*CDK9*) state.

To test for this possibility, we functionally assessed BAY-299–treated NK-tumor cell co-cultures. BAY-299 led to increased IFNγ production by the NK cells alone and at even higher levels when in co-culture with the HGSC cell line OVCAR8 or organoid line 17-116 (47), indicating increased immune activity (**Fig. 7D**; Supplementary Fig. S14D). Accordingly, paired flow cytometry analysis of the NK cells after BAY-299 treatment either alone or in co-culture demonstrated increased IFNγ$^+$, Ki67$^+$/IFNγ$^+$ double-positive cells, and CD107A$^+$ NK cells, more pronounced when these cells were cultured with OVCAR8 or organoid tumor cells (**Fig. 7E**; Supplementary Fig. S14E). Finally, BAY-299 increased tumor cell killing over vehicle in KHYG1 and OVCAR8 cell co-cultures (**Fig. 7F**). Altogether, these results indicate that BAY-299 induced chromatin remodeling causes a more cytotoxic and active state in NK cells *in vitro* and begs the question of whether BAY-299 can lead to enhanced anti-tumor killing by NK and possibly other cytotoxic immune cells *in vivo*.

BRD1 inhibition by BAY-299 shows efficacy *in vivo*

To assess BRD1 inhibitor efficacy *in vivo*, BAY-299 was tested in a syngeneic PAX8-positive ovarian cancer mouse model generated with STOSE cells (21). A MTD study was performed in female FVB/N mice. The drug was well tolerated with no side effects at the maximum dose.

For the *in vivo* experiment (**Fig. 7G**, top), 20 FVB/N female mice were injected with STOSE cells on day 1, and 18 days later, daily vehicle or BAY-299 treatments were initiated. Eighteen days after treatment initiation the mice were weighed, euthanized, and the tumor burden and immune composition analyzed (**Fig. 7G**).

Final animal weights were similar in both treatment groups (Supplementary Fig. S15A). Grossly visible solid tumor was dissected from all animals and appeared histologically similar in both groups forming sheets and clusters of neoplastic epithelioid cells with cytomorphologic features consistent with a poorly differentiated Müllerian carcinoma (Supplementary Fig. S15B). Tumor volumes were given a score of 0–3 (3 being highest), and most of the vehicle-treated mice scored highest while the majority of the BAY-299 scored lowest (**Fig. 7H**). Most of the vehicle-treated animals had high volume ascites correlating with high solid tumor burden, while most of the BAY-299–treated animals had little to no ascites correlating with low tumor burden (**Fig. 7I**).

We characterized solid tumors, ascites, and spleens for immune composition (T- and NK-cell quantity), exhaustion marker expression (TIM3, PD-1, and PD-L1), and activation marker expression (IFNγ, GZMB, Ki67; **Fig. 7J**; and **K**; Supplementary Fig. S15C–S15I). Given the low tumor burden and ascites volume in BAY-299–treated animals, samples were combined from multiple animals for analysis for each individual tissue/treatment type. Flow cytometry analysis of the spleens did not demonstrate shifts in T- or NK-cell populations (Supplementary Fig. S15C and S15E).

Flow cytometry analysis of the solid tumors demonstrated an increase in NK cells and CD8 T cells after BAY-299 treatment (**Fig. 7J**). NK-cell antibodies for markers NK-1.1 and NKp46 were utilized (48) with limited overlap in the CD3$^-$/NK-1.1$^+$ and CD3$^-$/NKp46$^+$ groups. The NKp46$^+$ NK cells expanded after BAY-299 treatment in the solid tumors (**Fig. 7J**; Supplementary Fig. S15F). Assessment of exhaustion markers post-treatment demonstrated a decrease in PD-1 expression on CD8 T and both NK-1.1 and NKp46$^+$ NK cells (**Fig. 7K**) similar to bispecific antibody (**Fig. 5**) and BAY-299 treatments (**Fig. 6**) in organoid co-cultures. TIM3 and PD-1/TIM3 coexpression and activation and killing marker expression was similar between treatments.

Conversely, in the ascites, only two BAY-299–treated samples showed CD8 T-cell expansion and NK-1.1$^+$ NK cells expanded post-treatment (Supplementary Fig. S15D and S15G). TIM3 expression decreased post-treatment on both NK-1.1 and NKp46$^+$ NK cells (Supplementary Fig. S15H) similar to the bispecific antibody (**Fig. 5**) and BAY-299 treatments (**Fig. 6**) in organoid co-cultures. TIM3 and PD-1/TIM3 coexpression was similar between treatments. Activation and killing markers were assessed, and CD107A mildly increased in both the NK-1.1 and NKp46$^+$ NK cells post-treatment (Supplementary Fig. S15I).

Altogether, these results suggest that *BRD1* depletion is likely an underlying mechanism for the superiority of the bispecific antibody and that, like the bispecific antibody, BRD1 inhibition leads to decreased immune exhaustion and increased immune activation, particularly in NK cells, which may make it an effective immune target in HGSC.

Discussion

The major cellular and mechanistic targets of ICB therapies in HGSC have not been defined making designing more effective therapies and identifying patients who might benefit from immune therapy difficult. Using real-time functional analysis of novel HGSC organoid-immune cell co-cultures treated with a novel bispecific antibody and its monospecific controls, we identified three critical cellular and mechanistic immune therapy targets in HGSC. This led to the identification of two novel immune therapies that may have increased activity in patients with HGSC, a bispecific anti-PD-1/PD-L1 antibody and BRD1 inhibitor, both of which show *in vivo* anti-tumor efficacy, suggesting further therapeutic exploration of these agents may be merited (**Fig. 7** and ref. 19).

Key to understanding the molecular functions of ICB agents in HGSC was our ability to gain a comprehensive appreciation of the effects of these agents on every cell in the tumor in novel HGSC organoid co-cultures (**Figs. 2**–**6**). Our most striking findings were in NK and T cells. Mechanisms of tumor microenvironment–induced NK-cell dysfunction and NK response to ICB agents are undefined (8, 16). We found that the bispecific antibody and the BRD1 inhibitor BAY-299 induced strong NK-cell activation through induction of a state change from an inert and exhausted to a more active and cytotoxic phenotype, which correlated with *in vivo* efficacy of these agents (**Figs. 2**, **4**–**7**; ref. 19). In so doing, we define NK-cell activation as a key component of therapeutic efficacy for immune therapy agents in HGSC that is lacking with currently used ICB agents.

In addition, our analysis demonstrated which CD8 T cells are most critical for ICB response in HGSC. We find that all three ICB agents, particularly the bispecific antibody, induced a transition from (i) naïve to cytotoxic progenitor-exhausted groups, and (ii) terminally exhausted to progenitor-exhausted cytotoxic groups (**Fig. 5**). This suggests that the ICB-driven naïve to cytotoxic progenitor transition may drive response in the long term and suggest that identifying therapies that can induce this state change may be important.

We determined that these state changes were being driven, in part, by bispecific antibody downregulation of *BRD1* expression (**Fig. 6**). Bromodomain proteins such as BRD1 and BRD4 play roles in immune and hematologic cell development and modulation of tumor inflammation (36, 37, 49) but are often targeted with the goal of affecting changes within the tumor cells as a means of therapeutic efficacy (38, 49, 50). Our findings led us to explore the novel role of BRD1 and BRD1 inhibitors in the immune cells instead.

Here we show BRD1 inhibition induces NK and some CD8 T cells into more active states by reducing exhaustion, and that this can enhance the activity of ICB agents like pembrolizumab *in vitro* (**Fig. 6**). The mechanism of action of BRD1 inhibition in these changes likely involves key epigenetic alterations (**Fig. 7A**–**C**); however, further work will be needed to fully understand this complex process. In addition, BAY-299 demonstrated increased efficacy in decreasing tumor burden *in vivo* through decreasing exhaustion of NK and CD8 T cells (**Fig. 7**). Overall, these findings suggest that BRD1 inhibition may be effective at enhancing the anti-tumor immune response and merit further exploration as a therapeutic option either alone or in relevant combinations in HGSC. In addition, this discovery in organoid co-cultures highlights the importance of studying the effects of any agent, even those thought to target intrinsic tumor cell properties, on every cell in a tumor. This may lead to unexpected discoveries that open up a broader array of small-molecule therapies in the immune space due to unanticipated effects of therapeutic agents on the immune compartment.

Overall, this work suggests the potential for HGSCs to be effectively targeted with immune therapies if the therapies engage the correct mechanistic pathways in the right immune cell types. These findings highlight a common immune therapy problem across HGSCs. It is not a tumor cell genomic or molecular defect making only some HGSCs responsive to these agents, rather it is a state of dysfunction in different subsets of CD8 T cells and NK cells driven by the solid tumor microenvironment blocking current ICB response across HGSCs. By gaining a better understanding of the mechanisms driving these dysfunctional states and how to overcome them, as we have begun to do here using a novel model system and novel therapeutic tool, we have identified available therapies to offer patients with HGSC, like BRD1 inhibitors, which effectively target these pathways. Mechanism-driven therapies have the potential to someday make immune therapy effective in HGSC, a deadly disease where it has not been effective before.

Authors' Disclosures

L.F. Al-Alem reports grants from Advanced Medical Research Foundation during the conduct of the study. U.M. Pandya reports grants from Advanced Medical Research Foundation during the conduct of the study. K. Boehnke is a current employee and shareholder of Eli Lilly and Company. D.T. Zarrella reports grants from Advanced Medical Research Foundation during the conduct of the study. U.A. Matulonis reports other funding from Merck outside the submitted work. B.R. Rueda reports grants from Advanced Medical Research Foundation during the conduct of the study and other funding from Palleon Pharmaceuticals and Siamab Therapeutics outside the submitted work. M. Brown reports grants from Novartis, personal fees and other compensation from Kronos Bio, GV20 Oncotherapy, and personal fees from H3 Biomedicine outside the submitted work. X.S. Liu reports grants from NIH during the conduct of the study, and X.S. Liu is a cofounder, board member, and consultant of GV20 Oncotherapy and its subsidiaries, SAB of 3DMedCare, consultant for Genentech, stockholder of BMY, TMO, WBA, ABT, ABBV, and JNJ, and receives research funding from Takeda and Sanofi. S.J. Hill reports grants from Eli Lilly and Company during the conduct of the study and grants from AstraZeneca outside the submitted work. No disclosures were reported by the other authors.

Authors' Contributions

C. Wan: Formal analysis, methodology, writing-original draft, writing-review and editing. **M.P. Keany:** Data curation, writing-original draft, writing-review and editing. **H. Dong:** Data curation, writing-original draft. **L.F. Al-Alem:** Resources, data curation, formal analysis, investigation, writing-review and editing. **U.M. Pandya:** Resources, data curation, formal analysis, investigation, writing-review and editing. **S. Lazo:** Data curation, writing-original draft, writing-review and editing. **K. Boehnke:** Data curation, writing-review and editing. **K.N. Lynch:** Data curation, investigation, writing-review and editing. **R. Xu:** Investigation, writing-review and editing. **D.T. Zarrella:** Investigation, writing-review and editing. **S. Gu:** Data curation, writing-original draft, writing-review and editing. **P. Cejas:** Resources, writing-review and editing. **K. Lim:** Resources, writing-review and editing. **H.W. Long:** Resources, writing-review and editing. **K.M. Elias:** Resources, writing-original draft, writing-review and editing. **N.S. Horowitz:** Resources, writing-original draft, writing-review and editing. **C.M. Feltmate:** Resources, writing-original draft, writing-review and editing. **M.G. Muto:** Resources, writing-original draft, writing-review and editing. **M.J. Worley:** Resources, writing-original draft, writing-review and editing. **R.S. Berkowitz:** Resources, writing-original draft, writing-review and editing. **U.A. Matulonis:** Resources, writing-review and editing. **M.R. Nucci:** Resources, writing-review and editing. **C.P. Crum:** Resources, writing-review and editing. **B.R. Rueda:** Resources, formal analysis, funding acquisition, investigation, writing-review and editing. **M. Brown:** Data curation, writing-review and editing. **X.S. Liu:** Data curation, writing-review and editing. **S.J. Hill:** Conceptualization, resources, data curation, formal analysis, supervision, funding acquisition, validation, investigation, visualization, methodology, writing-original draft, project administration, writing-review and editing.

Acknowledgments

We would like to express our gratitude to all the patients who donated tissue for this work. LY3300054, LY3434172, and the IgG control used in this work were provided by Eli Lilly and Company.

S.J. Hill was supported by the 2019 AACR-AstraZeneca Ovarian Cancer Research Fellowship (grant number 19-40-12-HILL), a DOD OCRP Pilot Award (W81XWH-19-1-0123), a Tina's Wish Rising Star grant, NIH K08 CA241093, NIH DP5 OD029637, and a sponsored research agreement from Eli Lilly and Company. B.R. Rueda was supported by the Advanced Medical Research Foundation and the Vincent Memorial Hospital Foundation. X.S. Liu was supported by NIH R01 CA234018. R. Xu was supported by the China Scholarship Council (grant number 201908610120). M. Brown was supported by a DOD OCRP Pilot Award (W81XWH-19-1-0147).

The costs of publication of this article were defrayed in part by the payment of page charges. This article must therefore be hereby marked *advertisement* in accordance with 18 U.S.C. Section 1734 solely to indicate this fact.

Received May 22, 2020; revised September 22, 2020; accepted November 3, 2020; published first November 6, 2020.

References

1. Siegel RL, Miller KD, Jemal A. Cancer statistics, 2019. CA Cancer J Clin 2019;69:7–34.
2. Narod S. Can advanced-stage ovarian cancer be cured? Nat Rev Clin Oncol 2016;13:255–61.
3. Ghisoni E, Imbimbo M, Zimmermann S, Valabrega G. Ovarian cancer immunotherapy: turning up the heat. Int J Mol Sci 2019;20:2927.
4. Odunsi K. Immunotherapy in ovarian cancer. Ann Oncol 2017;28:viii1–viii7.
5. Thorsson V, Gibbs DL, Brown SD, Wolf D, Bortone DS, Ou Yang TH, et al. The immune landscape of cancer. Immunity 2018;48:812–30.e14.
6. Sato E, Olson SH, Ahn J, Bundy B, Nishikawa H, Qian F, et al. Intraepithelial CD8+ tumor-infiltrating lymphocytes and a high CD8+/regulatory T cell ratio are associated with favorable prognosis in ovarian cancer. Proc Natl Acad Sci U S A 2005;102:18538–43.
7. Zhang L, Conejo-Garcia JR, Katsaros D, Gimotty PA, Massobrio M, Regnani G, et al. Intratumoral T cells, recurrence, and survival in epithelial ovarian cancer. N Engl J Med 2003;348:203–13.
8. Hoogstad-van Evert JS, Bekkers R, Ottevanger N, Jansen JH, Massuger L, Dolstra H. Harnessing natural killer cells for the treatment of ovarian cancer. Gynecol Oncol 2020;157:810–6.
9. Hoogstad-van Evert JS, Maas RJ, van der Meer J, Cany J, van der Steen S, Jansen JH, et al. Peritoneal NK cells are responsive to IL-15 and percentages are correlated with outcome in advanced ovarian cancer patients. Oncotarget 2018;9:34810–20.
10. Miller BC, Sen DR, Al Abosy R, Bi K, Virkud YV, LaFleur MW, et al. Subsets of exhausted CD8(+) T cells differentially mediate tumor control and respond to checkpoint blockade. Nat Immunol 2019;20:326–36.
11. Yost KE, Satpathy AT, Wells DK, Qi Y, Wang C, Kageyama R, et al. Clonal replacement of tumor-specific T cells following PD-1 blockade. Nat Med 2019;25:1251–9.
12. Wherry EJ, Kurachi M. Molecular and cellular insights into T cell exhaustion. Nat Rev Immunol 2015;15:486–99.
13. da Silva IP, Gallois A, Jimenez-Baranda S, Khan S, Anderson AC, Kuchroo VK, et al. Reversal of NK-cell exhaustion in advanced melanoma by Tim-3 blockade. Cancer Immunol Res 2014;2:410–22.
14. Thommen DS, Schumacher TN. T cell dysfunction in cancer. Cancer Cell 2018;33:547–62.
15. Philip M, Fairchild L, Sun L, Horste EL, Camara S, Shakiba M, et al. Chromatin states define tumour-specific T cell dysfunction and reprogramming. Nature 2017;545:452–6.
16. Sun H, Sun C. The rise of NK cell checkpoints as promising therapeutic targets in cancer immunotherapy. Front Immunol 2019;10:2354.
17. Jenkins RW, Aref AR, Lizotte PH, Ivanova E, Stinson S, Zhou CW, et al. *Ex vivo* profiling of PD-1 blockade using organotypic tumor spheroids. Cancer Discov 2018;8:196–215.
18. Neal JT, Li X, Zhu J, Giangarra V, Grzeskowiak CL, Ju J, et al. Organoid modeling of the tumor immune microenvironment. Cell 2018;175:1972—88.e16.
19. Kotanides H, Li Y, Malabunga M, Carpenito C, Eastman SW, Shen Y, et al. Bispecific targeting of PD-1 and PD-L1 enhances T-cell activation and antitumor immunity. Cancer Immunol Res 2020;8:1300–10.
20. Stoeckius M, Zheng S, Houck-Loomis B, Hao S, Yeung BZ, Mauck WM 3rd, et al. Cell Hashing with barcoded antibodies enables multiplexing and doublet detection for single cell genomics. Genome Biol 2018;19:224.
21. McCloskey CW, Goldberg RL, Carter LE, Gamwell LF, Al-Hujaily EM, Collins O, et al. A new spontaneously transformed syngeneic model of high-grade serous ovarian cancer with a tumor-initiating cell population. Front Oncol 2014;4:53.
22. Gitto SB, Kim H, Rafail S, Omran DK, Medvedev S, Kinose Y, et al. An autologous humanized patient-derived-xenograft platform to evaluate immunotherapy in ovarian cancer. Gynecol Oncol 2020;156:222–32.
23. Friese C, Harbst K, Borch TH, Westergaard MCW, Pedersen M, Kverneland A, et al. CTLA-4 blockade boosts the expansion of tumor-reactive CD8(+) tumor-infiltrating lymphocytes in ovarian cancer. Sci Rep 2020;10:3914.
24. Balkwill FR, Mantovani A. Cancer-related inflammation: common themes and therapeutic opportunities. Semin Cancer Biol 2012;22:33–40.
25. Li Y, Carpenito C, Wang G, Surguladze D, Forest A, Malabunga M, et al. Discovery and preclinical characterization of the antagonist anti-PD-L1 monoclonal antibody LY3300054. J Immunother Cancer 2018;6:31.
26. Zamarin D, Burger RA, Sill MW, Powell DJ Jr, Lankes HA, Feldman MD, et al. Randomized phase II trial of nivolumab versus nivolumab and ipilimumab for recurrent or persistent ovarian cancer: an NRG oncology study. J Clin Oncol 2020;38:1814–23.
27. Labrijn AF, Janmaat ML, Reichert JM, Parren P. Bispecific antibodies: a mechanistic review of the pipeline. Nat Rev Drug Discov 2019;18:585–608.
28. Ayers M, Lunceford J, Nebozhyn M, Murphy E, Loboda A, Kaufman DR, et al. IFN-gamma-related mRNA profile predicts clinical response to PD-1 blockade. J Clin Invest 2017;127:2930–40.
29. Stuart T, Butler A, Hoffman P, Hafemeister C, Papalexi E, Mauck WM 3rd, et al. Comprehensive integration of single-cell data. Cell 2019;177:1888–902.e21.
30. Romee R, Rosario M, Berrien-Elliott MM, Wagner JA, Jewell BA, Schappe T, et al. Cytokine-induced memory-like natural killer cells exhibit enhanced responses against myeloid leukemia. Sci Transl Med 2016;8:357ra123.
31. Del Zotto G, Marcenaro E, Vacca P, Sivori S, Pende D, Della Chiesa M, et al. Markers and function of human NK cells in normal and pathological conditions. Cytometry B Clin Cytom 2017;92:100–14.
32. Dong H, Adams NM, Xu Y, Cao J, Allan DSJ, Carlyle JR, et al. The IRE1 endoplasmic reticulum stress sensor activates natural killer cell immunity in part by regulating c-Myc. Nat Immunol 2019;20:865–78.
33. Morvan MG, Lanier LL. NK cells and cancer: you can teach innate cells new tricks. Nat Rev Cancer 2016;16:7–19.
34. Loftus RM, Assmann N, Kedia-Mehta N, O'Brien KL, Garcia A, Gillespie C, et al. Amino acid-dependent cMyc expression is essential for NK cell metabolic and functional responses in mice. Nat Commun 2018;9:2341.
35. Haghverdi L, Buettner F, Theis FJ. Diffusion maps for high-dimensional single-cell analysis of differentiation data. Bioinformatics 2015;31:2989–98.
36. Mishima Y, Miyagi S, Saraya A, Negishi M, Endoh M, Endo TA, et al. The Hbo1-Brd1/Brpf2 complex is responsible for global acetylation of H3K14 and required for fetal liver erythropoiesis. Blood 2011;118:2443–53.
37. Mishima Y, Wang C, Miyagi S, Saraya A, Hosokawa H, Mochizuki-Kashio M, et al. Histone acetylation mediated by Brd1 is crucial for Cd8 gene activation during early thymocyte development. Nat Commun 2014;5:5872.
38. Bouche L, Christ CD, Siegel S, Fernandez-Montalvan AE, Holton SJ, Fedorov O, et al. Benzoisoquinolinediones as potent and selective inhibitors of BRPF2 and TAF1/TAF1L bromodomains. J Med Chem 2017;60:4002–22.
39. Li B, Severson E, Pignon JC, Zhao H, Li T, Novak J, et al. Comprehensive analyses of tumor immunity: implications for cancer immunotherapy. Genome Biol 2016;17:174.
40. Jin HT, Anderson AC, Tan WG, West EE, Ha SJ, Araki K, et al. Cooperation of Tim-3 and PD-1 in CD8 T-cell exhaustion during chronic viral infection. Proc Natl Acad Sci U S A 2010;107:14733–8.
41. Yagita M, Huang CL, Umehara H, Matsuo Y, Tabata R, Miyake M, et al. A novel natural killer cell line (KHYG-1) from a patient with aggressive natural killer cell leukemia carrying a p53 point mutation. Leukemia 2000;14:922–30.

42. Hafner M, Niepel M, Chung M, Sorger PK. Growth rate inhibition metrics correct for confounders in measuring sensitivity to cancer drugs. Nat Methods 2016;13:521–7.
43. Wang D, Malarkannan S. Transcriptional regulation of natural killer cell development and functions. Cancers 2020;12:1591.
44. Hertweck A, Evans CM, Eskandarpour M, Lau JC, Oleinika K, Jackson I, et al. T-bet activates Th1 genes through mediator and the super elongation complex. Cell Rep 2016;15:2756–70.
45. Zhang H, Pandey S, Travers M, Sun H, Morton G, Madzo J, et al. Targeting CDK9 reactivates epigenetically silenced genes in cancer. Cell 2018;175:1244–58.e26.
46. Yang C, Siebert JR, Burns R, Zheng Y, Mei A, Bonacci B, et al. Single-cell transcriptome reveals the novel role of T-bet in suppressing the immature NK gene signature. Elife 2020;9:e51339.
47. Hill SJ, Decker B, Roberts EA, Horowitz NS, Muto MG, Worley MJ Jr, et al. Prediction of DNA repair inhibitor response in short-term patient-derived ovarian cancer organoids. Cancer Discov 2018; 8:1404–21.
48. Walzer T, Blery M, Chaix J, Fuseri N, Chasson L, Robbins SH, et al. Identification, activation, and selective *in vivo* ablation of mouse NK cells via NKp46. Proc Natl Acad Sci U S A 2007;104:3384–9.
49. White ME, Fenger JM, Carson WE 3rd. Emerging roles of and therapeutic strategies targeting BRD4 in cancer. Cell Immunol 2019; 337:48–53.
50. Sun C, Yin J, Fang Y, Chen J, Jeong KJ, Chen X, et al. BRD4 inhibition is synthetic lethal with PARP inhibitors through the induction of homologous recombination deficiency. Cancer Cell 2018;33:401–16.e8.